
DEEP GRAPH-LEVEL ORTHOGONAL HYPERSPHERE COMPRESSION FOR ANOMALY DETECTION

A PREPRINT

Yunhe Zhang[†]

Shenzhen Research Institute of Big Data
Shenzhen, China, 518172
zhangyhannie@gmail.com

Yan Sun[†]

School of Data Science
The Chinese University of Hong Kong, Shenzhen
Shenzhen, China, 518172
yansun@link.cuhk.edu.cn

Jinyu Cai

College of Computer and Data Science
Fuzhou University, Fujian, China, 350108
Shenzhen Research Institute of Big Data
Shenzhen, China, 518172
jinyucai1995@gmail.com

Jicong Fan^{*}

School of Data Science
The Chinese University of Hong Kong, Shenzhen
Shenzhen Research Institute of Big Data
Shenzhen, China, 518172
fanjicong@cuhk.edu.cn

February 14, 2023

ABSTRACT

Graph-level anomaly detection aims to identify anomalous graphs from a collection of graphs in an unsupervised manner. A common assumption of anomaly detection is that a reasonable decision boundary has a hypersphere shape, but may appear some non-conforming phenomena in high dimensions. Towards this end, we firstly propose a novel deep graph-level anomaly detection model, which learns the graph representation with maximum mutual information between substructure and global structure features while exploring a hypersphere anomaly decision boundary. The idea is to ensure the training data distribution consistent with the decision hypersphere via an orthogonal projection layer. Moreover, we further perform the bi-hypersphere compression to emphasize the discrimination of anomalous graphs from normal graphs. Note that our method is not confined to graph data and is applicable to anomaly detection of other data such as images. The numerical and visualization results on benchmark datasets demonstrate the effectiveness and superiority of our methods in comparison to many baselines and state-of-the-arts.

Keywords Anomaly Detection · Graph-level Learning · Graph Neural Network · Hypersphere Compression

1 Introduction

Anomaly detection is an essential task with various applications, such as detecting abnormal patterns or actions in credit-card fraud, medical diagnosis, sudden natural disasters [Aggarwal, 2017], etc. In some directions of anomaly detection, the training set only contains normal data and is used to train a model that can distinguish unusual patterns from abnormal ones [Pang et al., 2021, Seliya et al., 2021]. Anomaly detection on tabular data and images has been extensively studied recently [Ruff et al., 2018, Goyal et al., 2020, Chen et al., 2022, Liznerski et al., 2021, Sohn et al., 2021]. In contrast, there is relatively little work on graph-level data despite the fact that graph anomaly detection is very useful in various problems, such as identifying abnormal communities in social networks or detecting unusual protein structures in biology experiments. Compared with other types of data, graph data is inherently complicated and rich in structural and relational information. The complexity of graph structure facilitates us to learn graph-level

^{*}Corresponding author. [†]Equal contribution.

representations with discriminative patterns in many supervised tasks (e.g. graph classification). As for graph-level anomaly detection, however, the intricate graph structure brings many obstacles to unsupervised learning.

Graph anomaly detection usually composes four families: anomalous edge [Ouyang et al., 2020, Xu et al., 2020], node [Zhu and Zhu, 2020, Bojchevski and Günnemann, 2018], sub-graph [Wang et al., 2018, Zheng et al., 2018], and graph-level detections [Zheng et al., 2019, Chalapathy et al., 2018]. Herein, the target of the graph-level algorithms is to explore a regular group pattern and distinguish the abnormal manifestations of the group. Group abnormal behaviors usually foreshadow some unusual events and thus play an important role in practical applications. In the past decades, few approaches have focused on graph-level anomaly detection because of the difficulty of representing graphs into feature vectors without any label information. Considering that graph kernel can measure the similarity between graphs and regard the result as a representation non-strictly or implicitly, graph anomaly detection task associated with it usually performs as two-stage, which cannot maintain the quality of representation learning while learning normal data patterns. We also find that One-Class Support Vector Machine (OCSVM) [Schölkopf et al., 1999] with graph kernels sometimes yields unsatisfying performances since graph kernels may not be effective enough to quantify the similarity between graphs (see Section 5). So there is a large room for improvement regarding graph anomaly detection to our best knowledge. Concerning end-to-end models, Ma et al. [2022] proposed a global and local knowledge distillation method for graph-level anomaly detection, which learns rich global and local normal pattern information by random joint distillation of graph and node representations. However, the method needs to train two graph convolutional networks jointly at a high time cost. Zhao and Akoglu [2021] combined the Deep Support Vector Data Description (Deep SVDD) objective function and graph isomorphism network to learn a hypersphere of normal samples. Qiu et al. [2022] also sought a hypersphere decision boundary and optimized the representations learned by k Graph Neural Networks (GNN) close to the reference GNN while maximizing the differences between k GNNs, but did not consider the relationship between the graph-level representation and node features. Collecting all approaches based on the hypersphere assumption in graph anomaly detection, we find that the practical decision region may be an ellipsoid, thus causing the error when the standard hypersphere evaluation is employed. Besides, our experiment and the empirical exploration Vershynin [2018] further confirm that the high-dimensional data sometimes may be more likely to locate in a bi-hypersphere region (also known as *soap-bubble* phenomenon).

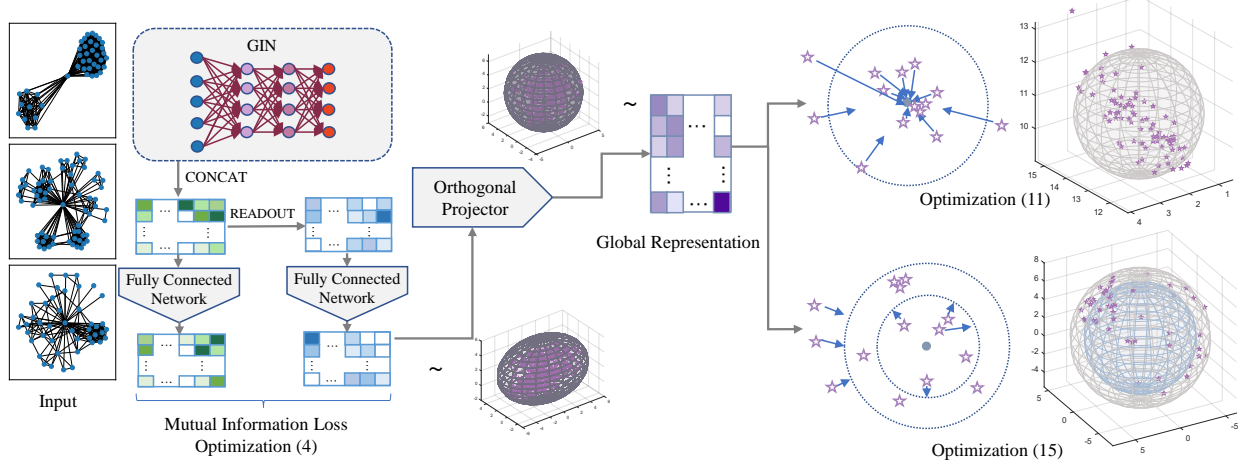


Figure 1: Architecture of the proposed models (right top: DOHSC; right bottom: DO2HSC).

In order to effectively explore a better representation without label information and obtain a more suitable decision boundary with high efficiency, in this paper, we propose a one-class deep graph-level anomaly detection method and its improved version. The first proposed model, **Deep Orthogonal Hypersphere Contraction** (DOHSC), uses the mutual information of local feature maps and the global representation to learn a high-quality representation and simultaneously optimizes it to distribute in a hypersphere area. An orthogonal projection layer then renders the decision region more hyperspherical and compact to decrease evaluation errors. With regard to *soap-bubble* phenomenon, an improved graph-level **Deep Orthogonal Bi-Hypersphere Compression** (DO2HSC) for anomaly detection architecture is proposed. From a cross-sectional point of view, DO2HSC limits the decision area (of normal data) to an interval enclosed by two co-centered hyperspheres and learns the orthogonality-projected representation similarly. The framework of the methods mentioned above is shown in Figure 1 correspondingly. Furthermore, we define a new evaluation way according to DO2HSC, and comprehensive experimental results verify the effectiveness of all proposed methods. In summary, our main contributions are listed as follows.

- First, we present a new graph-level hypersphere contraction algorithm for anomaly detection tasks, which is jointly trained via mutual information loss between local and global representations and hypersphere decision loss.
- Second, we impose an orthogonal projection layer on the proposed model to promote training data distribution close to the standard hypersphere, thus avoiding errors arising from inconsistencies between assessment criteria and actual conditions.
- Third, we propose the graph-level deep orthogonal bi-hypersphere compression model to further explore a decision region enclosed by two co-centered hyperspheres, which can effectively prevent anomalous data from falling close to the hyperspherical center and surpass baselines significantly in the experiments.
- Finally, the proposed methods are also applicable to and very effective on non-graph data (e.g. image).

2 Proposed Approach

In this section, we first introduce a joint learning architecture in detail, named graph-level Deep Orthogonal Hypersphere Compression. Then an improved algorithm is proposed to compensate for deficiency of the underlying assumption.

2.1 Graph-Level Deep Orthogonal Hypersphere Contraction

2.1.1 Vallina Model

Given a set of graphs $\mathbb{G} = \{G_1, \dots, G_N\}$ with N samples, the proposed model aims to learn a k -dimensional representation and then set a soft-boundary according to it. In this paper, the Graph Isomorphism Network (GIN) [Xu et al., 2019] is employed to obtain the graph representation in three stages: first, input the graph data and integrate neighbors of the current node (AGGREGATE); second, combine neighbor and current node features (CONCAT); finally, integrate all node information (READOUT) into one global representation. Mathematically, the i -th node features of l -th layer and the global features of its affiliated j -th graph would be denoted as

$$\begin{aligned} \mathbf{z}_\Phi^i &= \text{CONCAT}(\{\mathbf{z}_i^{(l)}\}_{l=1}^L), \\ \mathbf{Z}_\Phi(G_j) &= \text{READOUT}(\{\mathbf{z}_\Phi^i\}_{i=1}^{|G_j|}), \end{aligned} \quad (1)$$

where $\mathbf{z}_\Phi^i \in \mathbb{R}^{1 \times k}$ and $\mathbf{Z}_\Phi(G_j) \in \mathbb{R}^{1 \times k}$. To integrate the contained information and enhance the differentiation between node-level and global-level representations, we append additional fully connected layers denoted as the forms $M_\Upsilon(\cdot)$ and $T_\Psi(\cdot)$, respectively, where Υ and Ψ are the parameters of the added layers. So the integrated node-level and graph-level representations are obtained via

$$\mathbf{h}_{\Phi, \Upsilon}^i := M_\Upsilon(\mathbf{z}_\Phi^i); \quad \mathbf{H}_{\Phi, \Psi}(G_j) := T_\Psi(\mathbf{Z}_\Phi(G_j)), \quad (2)$$

To better capture the local information, we utilize the batch optimization property of neural networks to maximize the mutual information (MI) between local and global representations in each batch $\mathbf{G} \subseteq \mathbb{G}$, which is defined by Sun et al. [2020] as the following term:

$$\hat{\Phi}, \hat{\Psi}, \hat{\Upsilon} = \arg \max_{\Phi, \Psi, \Upsilon} I_{\Phi, \Psi, \Upsilon}(\mathbf{h}_{\Phi, \Upsilon}, \mathbf{H}_{\Phi, \Psi}(\mathbf{G})). \quad (3)$$

Specifically, the mutual information estimator $I_{\Phi, \Psi, \Upsilon}$ follows Jensen-Shannon MI estimator [Nowozin et al., 2016] with a positive-negative sampling method as below,

$$\begin{aligned} &I_{\Phi, \Psi, \Upsilon}(\mathbf{h}_{\Phi, \Upsilon}, \mathbf{H}_{\Phi, \Psi}(\mathbf{G})) \\ &:= \sum_{G_j \in \mathbf{G}} \frac{1}{|G_j|} \sum_{u \in G_j} I_{\Phi, \Psi, \Upsilon}(\mathbf{h}_{\Phi, \Upsilon}^u(G_j), \mathbf{H}_{\Phi, \Psi}(\mathbf{G})) \\ &= \sum_{G_j \in \mathbf{G}} \frac{1}{|G_j|} \sum_{u \in G_j} \left[\mathbb{E}(-\sigma(-\mathbf{h}_{\Phi, \Upsilon}^u(\mathbf{x}^+) \times \mathbf{H}_{\Phi, \Psi}(\mathbf{x}))) - \mathbb{E}(\sigma(\mathbf{h}_{\Phi, \Upsilon}^u(\mathbf{x}^-) \times \mathbf{H}_{\Phi, \Psi}(\mathbf{x}))) \right], \end{aligned} \quad (4)$$

where a softplus function $\sigma(z) = \log(1 + e^z)$ is activated after vector multiplication between node and graph representations. For \mathbf{x} as an input sample graph, we calculate the expected mutual information with its positive samples \mathbf{x}^+ and negative samples \mathbf{x}^- , which are generated from distribution across all graphs in a subset. Given each $G = (\mathcal{V}_G, \mathcal{E}_G)$ and node set $\mathcal{V}_G = \{v_i\}_{i=1}^{|G|}$, the positive and negative samples are divided in this way:

$$\mathbf{x}^+ = \begin{cases} \mathbf{x}_{ij}, & \text{if } v_i \in G_j, \\ 0, & \text{otherwise.} \end{cases} \quad (5)$$

And \mathbf{x}^- produces the opposite result in each of the conditions above. In the next step, a data-enclosing decision boundary is required for our anomaly detection task. According to the assumption that most normal data can locate in a hypersphere, the center of this decision boundary should be initialized through

$$\mathbf{c} = \frac{1}{N} \sum_{i=1}^N \mathbf{H}_{\Phi, \Psi}(G_i). \quad (6)$$

With this center, we expect to optimize the learned representation of normal data to be distributed as close to it as possible, so that the unexpected anomalous data falling out of this hypersphere would be detected. Besides, the regularization term is adopted to avoid over-fitting problems. Collectively denote the weight parameters of Φ , Ψ and Υ as $\mathcal{Q} := \Phi \cup \Psi \cup \Upsilon$, we formulate the training loss with two joint objectives – Hypersphere Contraction and MI:

$$\min_{\Phi, \Psi, \Upsilon} \frac{1}{|\mathbf{G}|} \sum_{i=1}^{|\mathbf{G}|} \|\mathbf{H}_{\Phi, \Psi}(G_i) - \mathbf{c}\|^2 + \lambda I_{\Phi, \Psi, \Upsilon}(\mathbf{h}_{\Phi, \Upsilon}, \mathbf{H}_{\Phi, \Psi}(\mathbf{G})) + \frac{\mu}{2} \sum_{\mathbf{Q} \in \mathcal{Q}} \|\mathbf{Q}\|_F^2, \quad (7)$$

where $|\mathbf{G}|$ denotes the number of graphs in batch \mathbf{G} and λ is a trade-off factor, the third term is a network weight decay regularizer with the hyperparameter μ .

2.1.2 Orthogonal Projection Layer

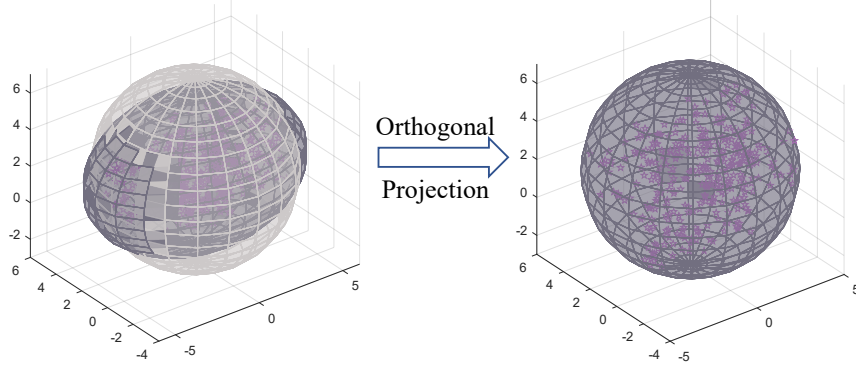


Figure 2: Illustration of decision boundaries with and without the orthogonal projection layer. In the left subfigure, the real decision region where training data are distributed may be an ellipsoid (dark grey). This contradicts with the hypersphere decision boundary (light grey) set by Equation 7. After orthogonal projection, the ellipsoid is expected to be transformed into a standard hypersphere, which avoids the evaluation error. *Note: Data is simulated.*

However, an empirical study shows that a hyperellipsoid is commonly observed during deep representation learning. This phenomenon would lead to inaccuracies in the final test because the evaluation results are based on the hypersphere decision region. The objective (7) obviously cannot guarantee the soft-boundary of learned representation to be a standard hypersphere like Figure 2. Accordingly, we append an orthogonal projection layer after obtaining the global representation. Note that we pursue orthogonal features of latent representation rather than computing the projection onto the column or row space of $\mathbf{H}_{\Phi, \Psi}$. This method is equivalent to performing Principal Component Analysis (PCA) [Wold et al., 1987] and using the standardized principal components. Our experiments also justify the necessity of this projection step and standardization process, which will be discussed further in Section 5.3 and Appendix H. Specifically, the projection layer can be formulated as

$$\tilde{\mathbf{H}}_{\Phi, \Psi, \Theta}(G) = \text{Proj}_{\Theta}(\mathbf{H}_{\Phi, \Psi}(G)) = \mathbf{H}_{\Phi, \Psi} \mathbf{W}, \text{ subject to } \tilde{\mathbf{H}}_{\Phi, \Psi, \Theta}^\top \tilde{\mathbf{H}}_{\Phi, \Psi, \Theta} = \mathbf{I}_{k'}, \quad (8)$$

where $\Theta := \{\mathbf{W} \in \mathbb{R}^{k' \times k'}\}$ are the projection parameters, $\mathbf{I}_{k'}$ denotes an identity matrix, and k' is the projected dimension. Note that to achieve (8), one may consider adding a regularization term $\frac{\alpha}{2} \|\tilde{\mathbf{H}}_{\Phi, \Psi, \Theta}^\top \tilde{\mathbf{H}}_{\Phi, \Psi, \Theta} - \mathbf{I}_{k'}\|_F^2$ with large enough α to the objective, which is not very effective and will lead to one more tuning hyperparameter. Instead, we propose to achieve (8) via singular value decomposition, i.e.

$$\mathbf{U} \Lambda \mathbf{V}^\top = \mathbf{H}_{\Phi, \Psi}, \quad \mathbf{W} := \mathbf{V}_{k'} \Lambda_{k'}^{-1} \quad (9)$$

where $\Lambda = \text{diag}(\rho_1, \rho_2, \dots, \rho_{|\mathbf{G}|})$ and \mathbf{V} are the diagonal matrix with singular values and right-singular matrix of $\mathbf{H}_{\Phi, \Psi}$, respectively. It needs to be emphasized that $\mathbf{V}_{k'} := [\mathbf{v}_1, \dots, \mathbf{v}_{k'}]$ denotes the first k' right-singular vectors and $\Lambda_{k'} := \text{diag}(\rho_1, \dots, \rho_{k'})$. In each forward propagation epoch, the original weight parameter is substituted to a new matrix \mathbf{W} in subsequent loss computations.

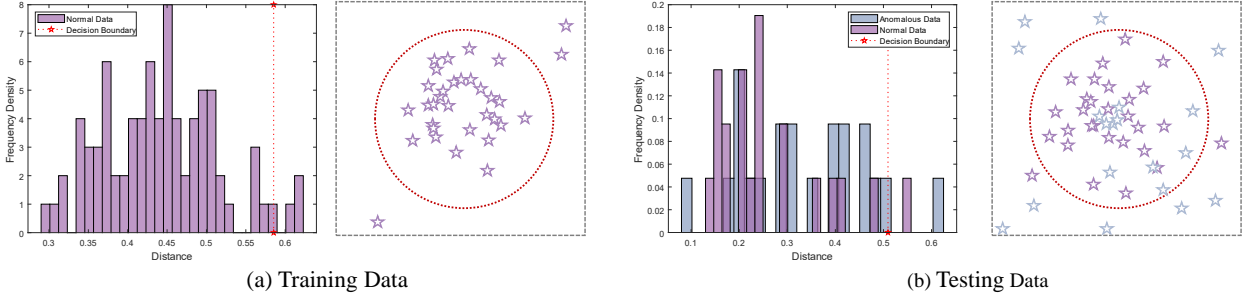


Figure 3: Illustration of inevitable flaws in DOHSC on both the training and testing data of COX2. Left: the ℓ_2 -norm distribution of 4-dimensional distances learned from the real dataset; Right: the pseudo-layout in two-dimensional space sketched by reference to the empirical distribution.

2.1.3 Anomaly Detection

Attaching with an orthogonal projection layer, the improved initialization of the center is rewritten in the following form

$$\tilde{\mathbf{c}} = \frac{1}{N} \sum_{i=1}^N \tilde{\mathbf{H}}_{\Phi, \Psi, \Theta}(G_i) \quad (10)$$

and the final objective function for anomaly detection tasks in a mini-batch would become

$$\min_{\Theta, \Phi, \Psi, \Upsilon} \frac{1}{|\mathbf{G}|} \sum_{i=1}^{|\mathbf{G}|} \|\tilde{\mathbf{H}}_{\Phi, \Psi, \Theta}(G_i) - \tilde{\mathbf{c}}\|^2 + \lambda \sum_{\mathbf{G} \in \mathcal{G}} I_{\Phi, \Psi, \Upsilon} \left(\mathbf{h}_{\Phi, \Upsilon}, \tilde{\mathbf{H}}_{\Phi, \Psi, \Theta}(\mathbf{G}) \right) + \frac{\mu}{2} \sum_{\mathbf{Q} \in \mathcal{Q}} \|\mathbf{Q}\|_F^2. \quad (11)$$

After the training stage, a decision boundary \hat{r} will be fixed, which is calculated based on the $1 - \nu$ percentile of the training data distance distribution:

$$\hat{r} = \arg \min_r \mathcal{P}(\mathbf{D} \leq r) \geq \nu \quad (12)$$

where $\mathbf{D} := \{d_i\}_{i=1}^N$ follows a sampled distribution \mathcal{P} , and $d_i = \|\tilde{\mathbf{H}}_{\Phi, \Psi, \Theta}(G_i) - \tilde{\mathbf{c}}\|$. Accordingly, the anomalous score of i -th instance is defined as follows:

$$s_i = d_i^2 - \hat{r}^2 \quad (13)$$

where $\mathbf{s} = (s_1, s_2, \dots, s_N)$. It is evident that when the score is positive, the instance is identified as abnormal, and the opposite is considered normal.

The detailed procedures of algorithm are summarized into Algorithm 1 (see Appendix A). It starts with graph representation learning and promotes the training data to approximate the center of a hypersphere while adding an orthogonal projection layer. Unfortunately, it can be observed from Figures 3 and 5 that the anomalous data would appear in partial regions of the learned decision hypersphere, which are not filled by the training data, especially the region close to the center. To explore this particular phenomenon and handle it, an improved graph-level anomaly detection approach, termed as graph-level Deep Orthogonal Bi-Hypersphere Compression (DO2HSC), is designed in the next section.

2.2 Graph-Level Deep Orthogonal Bi-Hypersphere Compression

2.2.1 Motivation and Theoretical Analysis

As aforementioned, we found that the learned distribution of training data sometimes does not conform the hypersphere assumption. Let the anomaly score be determined by ℓ_2 norm $\|\mathbf{z} - \mathbf{c}\|$ where \mathbf{c} denotes the centroid, the original evaluation of anomaly detection is to compare the score with a threshold \hat{r} determined by a certain quantile (e.g. 0.95). Specifically, if $\|\mathbf{z} - \mathbf{c}\| \geq \hat{r}$ then \mathbf{z} is abnormal. So it is natural to expect most samples to locate near the origin. However, the empirical exploration found that in a high dimensional space, most samples are far away from the origin. Taking Gaussian distributions as an example, the distributions would look like a *soap-bubble*², which means the high-dimensional normal data are more likely to locate in a bi-hypersphere instead of a simple hypersphere [Vershynin, 2018]. To be more specific, referred to [Vershynin, 2018], the typical set, where data has information closest to the

²<https://www.inference.vc/high-dimensional-gaussian-distributions-are-soap-bubble/>

expected entropy of the population, of a Gaussian is the thin shell within a distance from the origin, just like the circumstances showed in Figure 4. The higher the dimensionality of the data, the further the sampled instance is from the center instead.

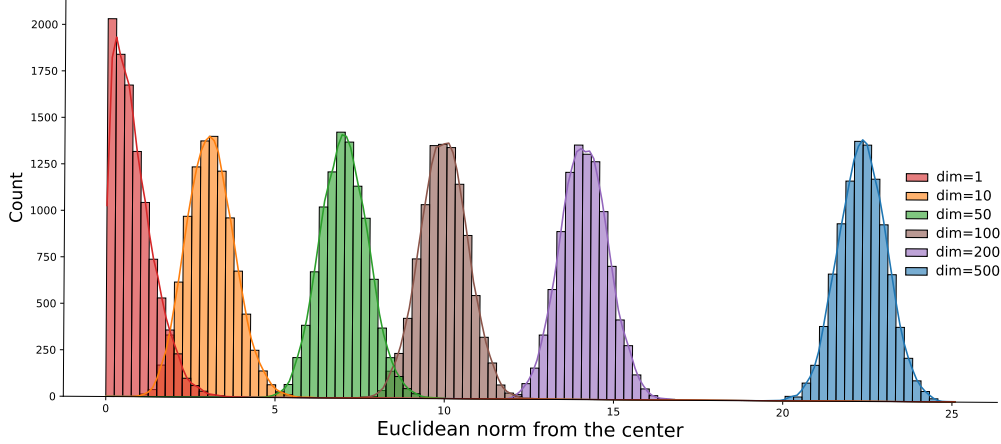


Figure 4: Histogram of distances (Euclidean norm) from the center of 10,000 random samples under (univariate or) high-dimensional Gaussian distributions $\mathcal{N}(\mathbf{0}, \mathbf{I})$.

To sum up, we formally formulate the following proposition and it can be easily derived from Lemma 1 of [Laurent and Massart, 2000].

Proposition 1. *Suppose $\mathbf{z}_1, \mathbf{z}_2, \dots, \mathbf{z}_n$ are sampled from $\mathcal{N}(\mathbf{0}, \mathbf{I}_d)$ independently. Then for any \mathbf{z}_i and all $t \geq 0$, the following inequality holds:*

$$\mathbb{P} \left[\|\mathbf{z}_i\| \geq \sqrt{d - 2\sqrt{dt}} \right] \geq 1 - e^{-t}.$$

The proposition proves that when the dimension is high, each \mathbf{z}_i is outside of a hypersphere of radius $r' := \sqrt{d - 2\sqrt{dt}}$, with probability at least $1 - e^{-t}$. When r' is closer to \hat{r} (refer to (12)), normal data are more likely away from the center (also can be seen in Figure 4).

It should be pointed out that in anomaly detection, \mathbf{z}_i (e.g. $\mathbf{z}_i = \tilde{\mathbf{H}}_{\Phi, \Phi, \Theta}(G_i)$ in Section 2.1.3) are not necessarily isotropic Gaussian. However, we have the following result.

Proposition 2. *Let $\mathbf{z}_i = \tilde{\mathbf{H}}_{\Phi, \Phi, \Theta}(G_i)$, $i = 1, \dots, N$ and let $f : \mathbb{R}^k \rightarrow \mathbb{R}^k$ be an η -Lipschitz function such that $\mathbf{s} = f(\mathbf{z})$ are isotropic Gaussian $\mathcal{N}(\bar{\mathbf{c}}, \mathbf{I}_k)$. Let \mathbf{c} be a predefined center of $\{\mathbf{z}_i\}_{i=1}^N$ and suppose $\|\bar{\mathbf{c}} - f(\mathbf{c})\| \leq \epsilon$. Then for any \mathbf{z}_i and all $t \geq 0$, the following inequality holds:*

$$\mathbb{P} \left[\|\mathbf{z}_i - \mathbf{c}\| \geq \eta^{-1} \left(\sqrt{k - 2\sqrt{kt}} - \epsilon \right) \right] \geq 1 - e^{-t}.$$

The proposition (proved in Appendix C) shows that most data (N') satisfy $\|\mathbf{z} - \mathbf{c}\| \geq r' := \eta^{-1} \left(\sqrt{k - 2\sqrt{kt}} - \epsilon \right)$ (with probability around $\binom{N}{N'} (1 - e^{-t})^{N'} e^{-t(N-N')}$) where r' is close to \hat{r} , which means the normality could not be supported by the training data within the range $[0, r']$. Therefore, it is justified that hypersphere anomaly detection tasks should be improved as the bi-hypersphere version.

2.2.2 Architecture of DO2HSC

Since DOHSC cannot detect anomalies close to the center, we propose an improved approach, DO2HSC, which sets the decision boundary as an interval region between two co-centered hyperspheres. This can narrow the decision area's scope so as to induce normal data to fill the entire interval area as much as possible. Also, it can better handle *soap-bubble* problems than DOHSC.

After the same graph representation learning stage, we firstly utilize the DOHSC model for a few epochs to initialize the large radius r_{\max} and the small radius r_{\min} of the interval area according to the $1 - \nu$ percentile and ν of the sample

distances distribution, respectively. The aforementioned descriptions can be denoted mathematically as below.

$$\begin{aligned} r_{\max} &= \arg \min_r \mathcal{P}(\mathbf{D} \leq r) \geq \nu, \\ r_{\min} &= \arg \min_r \mathcal{P}(\mathbf{D} \leq r) \geq 1 - \nu. \end{aligned} \quad (14)$$

After fixing the decision boundaries r_{\max} and r_{\min} , the training loss is also set with a trade-off factor λ , which implicitly controls the importance of the max-min term:

$$\min_{\Theta, \Phi, \Psi, \Upsilon} \frac{1}{|\mathbf{G}|} \sum_{i=1}^{|\mathbf{G}|} (\max\{d_i, r_{\max}\} - \min\{d_i, r_{\min}\}) + \lambda \sum_{\mathbf{G} \in \mathbb{G}} I_{\Phi, \Psi, \Upsilon} \left(\mathbf{h}_{\Phi, \Upsilon}, \tilde{\mathbf{H}}_{\Phi, \Psi, \Theta}(\mathbf{G}) \right) + \frac{\mu}{2} \sum_{\mathbf{Q} \in \mathcal{Q}} \|\mathbf{Q}\|_F^2. \quad (15)$$

This decision loss has the lowest bound $r_{\max} - r_{\min}$ and can be jointly minimized with mutual information effectively. Besides, the evaluation standard of test data is also needed to change based on this interval structure. More specifically, all instances located in the inner hypersphere and out of the outer hypersphere should be identified as anomalous graphs; only those located in the interval area should be regarded as normal data. Compared with (13), we reset a new score function to award the positive samples beyond $[r_{\min}, r_{\max}]$ and meanwhile punishing the negative samples within the range. Accordingly, the distinctive scores are calculated by

$$s_i = (d_i - r_{\max}) \cdot (d_i - r_{\min}), \quad (16)$$

where $i \in \{1, \dots, N\}$. This way, we can also effectively identify a sample's abnormality by its score. In general, the improved deep graph-level anomaly detection algorithm changes the decision boundary and effectively makes the normal area more compact. Correspondingly, the new practical evaluation is raised to adapt to the improved detection way. Eventually, we summarize the detailed procedures of the optimization into Algorithm 2 (please see Appendix A).

3 Connections with Previous Work

As one of the classic one-class anomaly detection algorithm, Deep SVDD Schölkopf et al. [1999] assumes that the specific shape of decision regions is a hypersphere. Considered that it is difficult to guarantee that the learned embedding representation's distribution perfectly fits the hypersphere hypothesis, we design the orthogonal projection layer to obtain an embedding representation that conforms as closely as possible to the standard assumption. This point also differs the proposed graph-level representation learning stage from infoGraph method Sun et al. [2020], which promotes the learned graph representation to better meet theoretical requirements. Due to the similar network architectures, we also clarify the differences between Zhao and Akoglu [2021] and ours. Zhao and Akoglu [2021] optimized one-class model based on Deep SVDD as the anomaly measure, which directly utilized the readout result of GIN for Deep SVDD module. Whereas, the involved mutual information loss in the proposed models can obtain the graph representation incorporating local and global information, and avoid trivial solutions when solving anomaly detection problems. Besides, like we mentioned above, we imposed an orthogonal projection layer to maintain consistency between the learned decision boundary and normal data distributions. Last but not least, a new method is presented to construct a more suitable decision region learned as a bi-hypersphere, between which normal data are accommodated and hence yield more space for anomalies. Bi-hypersphere assumption has not been studied in the anomaly detection field to our best knowledge. It is the first exploration and provides a new perspective for future detection works. More related works are summarized in Appendix D.

4 Generalization to Other Data Types

The methods above can also be generalized to non-graph types of data, such as tabular or image data. To tackle these datasets, the graph representation learning module is replaced by a common representation learning module. We still keep the proposed orthogonal projection layer but remove mutual information loss. Then the objective functions of DOHSC and DO2HSC will become the following forms:

$$\min_{\mathcal{W}, \Theta} \frac{1}{n} \sum_{i=1}^n \|\text{Proj}_{\Theta}(f_{\text{enc}}(\mathbf{x}_i, \mathcal{W})) - \tilde{\mathbf{c}}\|^2 + \frac{\lambda}{2} \sum_{l=1}^L \|\mathbf{W}^l\|_F^2, \quad (17)$$

$$\min_{\mathcal{W}, \Theta} \frac{1}{n} \sum_{i=1}^n (\max\{d_i, r_{\max}\} - \min\{d_i, r_{\min}\}) + \frac{\lambda}{2} \sum_{l=1}^L \|\mathbf{W}^l\|_F^2 \quad (18)$$

where f_{enc} means the representation learning module (just like an encoder architecture) with the parameter set $\mathcal{W} = \{\mathbf{W}^l\}_{l=1}^L$ and $d_i = \|\text{Proj}_{\Theta}(f_{\text{enc}}(\mathbf{x}_i, \mathcal{W})) - \tilde{\mathbf{c}}\|$. After the representation learning stage, the subsequent anomaly detection evaluation procedures are implemented according to Section 2.1.3 and Section 2.2.2.

5 Experiments on Graph Data

5.1 Experiment Setting

Datasets: We evaluate our models on six real-world graph datasets³ (COLLAB, COX2, ER_MD, MUTAG, DD and IMDB-Binary), which are converted from graph classification benchmarks for GAD tasks. We follow the standard one-class experimental settings and data-split method in previous work [Zhao and Akoglu, 2021, Qiu et al., 2022]. The details of datasets are shown in Appendix E.

Baselines: We compare our methods with the following unsupervised graph-level anomaly detection methods, including four graph kernels combined with OCSVM and four state-of-the-art baselines: Random Walk (RW) [Gärtner et al., 2003, Kashima et al., 2003], Shortest Path Kernel (SP) [Borgwardt and Kriegel, 2005], Weisfeiler-Lehman Sub-tree Kernel (WL) [Shervashidze et al., 2011] and Neighborhood Hash Kernel (NH) [Hido and Kashima, 2009], Deep One Class Model with GIN network (OCGIN) [Zhao and Akoglu, 2021], Graph-level embedding Learning via Mutual Information Maximization+Deep SVDD (infoGraph+Deep SVDD) [Sun et al., 2020, Ruff et al., 2018], Global and Local Knowledge Distillation for Graph-level Anomaly Detection (GLocalKD) [Ma et al., 2022] and One-Class Graph Transformation Learning (OCGTL) [Qiu et al., 2022].

5.2 Results

In this section, the averages and standard deviations of the Area Under Operating Characteristic Curve (AUC) are used to support the comparable experiments by repeating each algorithm ten times. Tables 1 and 2 report the mean AUC and its standard deviations. It can be seen that the proposed methods basically achieve the best AUC values compared to other algorithms on all datasets. Both approaches outperform other state-of-the-art baselines, and DO2HSC obtains superior performance and get 5% higher performance than other algorithms on many datasets, such as MUTAG, COLLAB Class 1, and ER_MD Class 0, IMDB-Binary Class 1, etc. It is worth mentioning that we defeat infoGraph+Deep SVDD with a large improvement, which is a degraded version of the proposed models, thus showing that promoting representation learning towards the anomaly detection goal is meaningful and well targeted. Besides, it can be seen that there exists a large improvement (exceeding 20%) on Class 1 of ER_MD between DOHSC and DO2HSC. An distance distribution visualization is given to prove their differences (see Figure 5).

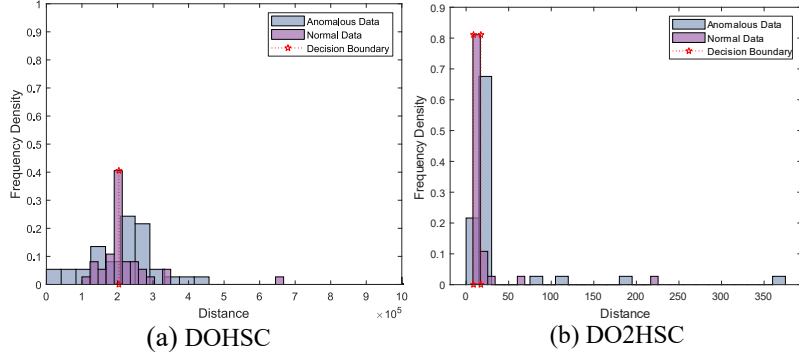


Figure 5: Distance distribution visualizations of DOHSC and DO2HSC on ER_MD dataset.

The anomaly detection visualization results of DO2HSC are displayed in Figure 6 and those of DOHSC are also shown in Appendix G. We draw them by setting the projection dimension to three directly. Results of different perspectives are given to avoid blind spots in the field of vision, demonstrating excellent performance. Hence, it can be concluded that the effect of the improved model is in line with our motivation and shows much potential.

5.3 Ablation Study

In this section, we display the ablation study of the orthogonal projection layer on three datasets. From quantitative comparisons in Table 3, we concluded that orthogonality positively influences all performance to some extent. It also well supports our assumption discussed in Section 2.1.2. Except for the aforementioned contents, please see the detailed experiment configurations, parameter sensitivity and robustness of the proposed models, supplemented visualizations of

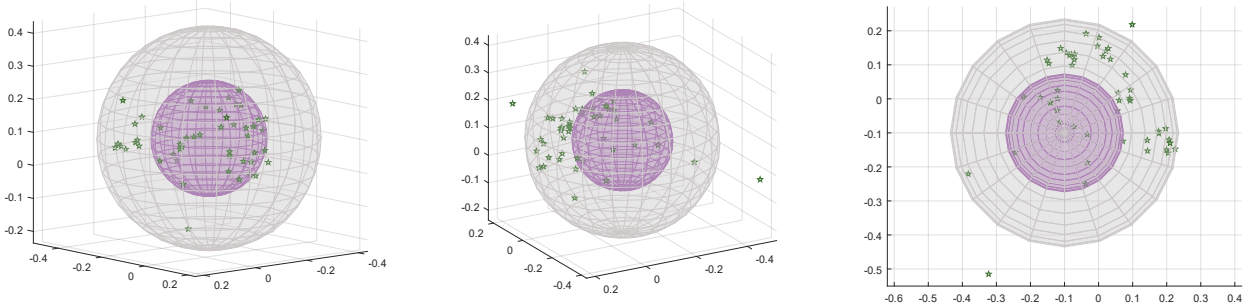
³<https://ls11-www.cs.tu-dortmund.de/staff/morris/graphkerneldatasets>

Table 1: Average AUCs with standard deviation (10 trials) of different graph-level anomaly detection algorithms. We assess models by regarding every data class as normal data, respectively. The best results are highlighted in **bold** and ‘-’ means out of memory.

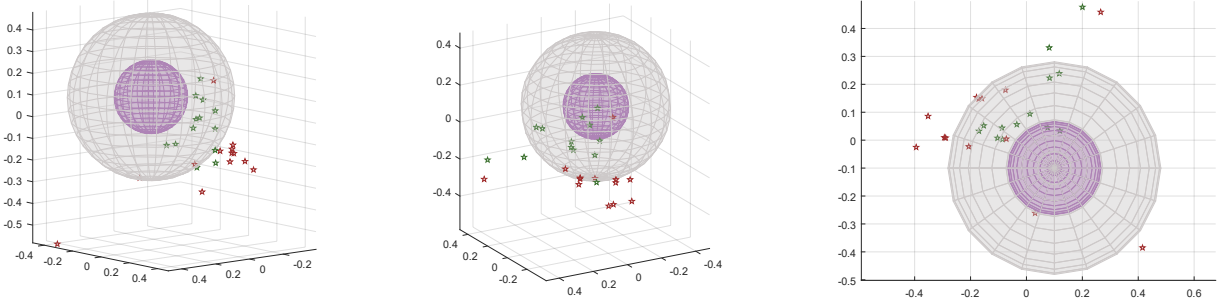
	COLLAB			COX2		ER_MD	
	0	1	2	0	1	0	1
SP+OCSVM	0.5910 \pm 0.0000	0.8397 \pm 0.0000	0.7902 \pm 0.0000	0.5408 \pm 0.0000	0.5760 \pm 0.0000	0.4092 \pm 0.0000	0.3824 \pm 0.0000
WL+OCSVM (optimal)	0.5122 \pm 0.0000	0.8054 \pm 0.0000	0.7996 \pm 0.0000	0.5990 \pm 0.0000	0.5057 \pm 0.0000	0.4571 \pm 0.0000	0.3262 \pm 0.0000
NH+OCSVM	0.5976 \pm 0.0000	0.8054 \pm 0.0000	0.6414 \pm 0.0000	0.4841 \pm 0.0000	0.4717 \pm 0.0000	0.5155 \pm 0.0200	0.3648 \pm 0.0000
RW+OCSVM	–	–	–	0.5243 \pm 0.0000	0.6553 \pm 0.0000	0.4820 \pm 0.0000	0.3484 \pm 0.0000
OCGIN	0.4217 \pm 0.0606	0.7565 \pm 0.2035	0.1906 \pm 0.0857	0.5964 \pm 0.0578	0.5683 \pm 0.0768	0.5645 \pm 0.0323	0.4358 \pm 0.0538
infoGraph+Deep SVDD	0.5662 \pm 0.0597	0.7926 \pm 0.0986	0.4062 \pm 0.0978	0.4825 \pm 0.0624	0.5029 \pm 0.0700	0.5312 \pm 0.1545	0.5682 \pm 0.0704
GLocalKD	0.4638 \pm 0.0003	0.4330 \pm 0.0016	0.4792 \pm 0.0004	0.3861 \pm 0.0131	0.3143 \pm 0.0383	0.5781 \pm 0.1790	0.7154 \pm 0.0000
OCGTL	0.6504 \pm 0.0433	0.8908 \pm 0.0239	0.4029 \pm 0.0541	0.5541 \pm 0.032	0.4862 \pm 0.0224	0.2755 \pm 0.0317	0.6915 \pm 0.0207
DOHSC (Ours)	0.9185 \pm 0.0455	0.9755 \pm 0.0030	0.5450 \pm 0.0469	0.6263 \pm 0.0333	0.6805 \pm 0.0168	0.6620 \pm 0.0308	0.5184 \pm 0.0793
DO2HSC (Ours)	0.6718 \pm 0.0353	0.9153 \pm 0.0070	0.7188 \pm 0.0260	0.6329 \pm 0.0292	0.6518 \pm 0.0481	0.6867 \pm 0.0226	0.7351 \pm 0.0159

Table 2: Average AUCs with standard deviation (10 trials) of different graph-level anomaly detection algorithms. We assess models by regarding every data class as normal data, respectively. The best results are highlighted in **bold** and ‘-’ means out of memory.

	MUTAG		DD		IMDB-Binary	
	0	1	0	1	0	1
SP+OCSVM	0.5917 \pm 0.0000	0.2608 \pm 0.0000	0.6856 \pm 0.0000	0.4474 \pm 0.0000	0.4592 \pm 0.0000	0.4716 \pm 0.0000
WL+OCSVM (optimal)	0.6509 \pm 0.0000	0.2960 \pm 0.0000	0.7397 \pm 0.0000	0.4946 \pm 0.0000	0.5157 \pm 0.0000	0.4607 \pm 0.0000
NH+OCSVM	0.7959 \pm 0.0274	0.1679 \pm 0.0062	0.7424 \pm 0.0000	0.3684 \pm 0.0000	0.5321 \pm 0.0000	0.4652 \pm 0.0000
RW+OCSVM	0.8698 \pm 0.0000	0.1504 \pm 0.0000	–	–	0.4951 \pm 0.0000	0.5311 \pm 0.0000
OCGIN	0.8491 \pm 0.0424	0.4933 \pm 0.1525	0.6659 \pm 0.0444	0.6003 \pm 0.0534	0.4047 \pm 0.1083	0.3332 \pm 0.0649
infoGraph+Deep SVDD	0.8805 \pm 0.0448	0.6166 \pm 0.2052	0.3942 \pm 0.0436	0.6484 \pm 0.0236	0.6353 \pm 0.0277	0.5836 \pm 0.0995
GLocalKD	0.3952 \pm 0.2258	0.2965 \pm 0.2641	0.1952 \pm 0.0000	0.2203 \pm 0.0001	0.5383 \pm 0.0124	0.4812 \pm 0.0101
OCGTL	0.6570 \pm 0.0210	0.7579 \pm 0.2212	0.6990 \pm 0.0260	0.6767 \pm 0.0280	0.6510 \pm 0.0180	0.6412 \pm 0.0127
DOHSC (Ours)	0.8822 \pm 0.0432	0.8115 \pm 0.0279	0.7083 \pm 0.0188	0.7579 \pm 0.0154	0.7160 \pm 0.0600	0.7705 \pm 0.0045
DO2HSC (Ours)	0.9089 \pm 0.0609	0.8250 \pm 0.0790	0.7320 \pm 0.0194	0.7651 \pm 0.0317	0.6406 \pm 0.0642	0.7101 \pm 0.0429



(a) Training Result



(b) Testing Result

Figure 6: 3D Visualization results of the DO2HSC on MUTAG Class 0 from different perspectives.

Table 3: Ablation study of the orthogonal projection layer (OPL). We test models by regarding every data class as normal data, respectively. The best performance is highlighted in **bold**.

	OPL	Class	MUTAG	COX2	IMDB-Binary
DOHSC	✗	0	0.8521	0.5817	0.5880
		1	0.8912	0.5737	0.6082
	✓	0	0.8639	0.6433	0.6192
		1	0.9088	0.6077	0.6830
DO2HSC	✗	0	0.8934	0.6281	0.6252
		1	0.7504	0.6178	0.6541
	✓	0	0.9467	0.7158	0.6933
		1	0.9184	0.7074	0.6700

distance distributions for anomaly detection and visualization comparison between proposed models with orthogonal projection layer and without orthogonal projection layer in Appendix H, which can also strongly support our theory and validate the effectiveness.

6 Experiments on non-graph data

6.1 Experiment Setting

Datasets: One image dataset (Fashion-MNIST) and two tabular datasets (Thyroid, Arrhythmia) are tested to verify the effectiveness of the proposed extension on non-graph data. Herein, we follow the data split settings in Zong et al. [2018] for both tabular datasets.

Baselines: We follow the work of [Ruff et al., 2018] and utilize the AUCs of three state-of-the-art anomaly detection algorithms Deep SVDD Ruff et al. [2018], deep robust one-class classification (DROCC) Goyal et al. [2020], and fully convolutional data description for explainable deep one-class classification (FCDD) Liznerski et al. [2021] on the image dataset, and the F1-scores of several compared methods OCSVM Schölkopf et al. [1999], classification-based anomaly detection for general data (GOAD) Bergman and Hoshen [2020], DROCC, local outlier factor for anomaly detection (LOF) Breunig et al. [2000], Deep SVDD and perturbation learning based anomaly detection (PLAD) Cai and Fan [2022]). Herein, some performance on tabular data is reported directly according to the following papers Goyal et al. [2020], Cai and Fan [2022], Bergman and Hoshen [2020]. Other compared methods are reproduced by their official codes. Note that the network architecture of Deep SVDD is set the same as ours so as to keep fairness.

6.2 Results

Table 4: Average F1-scores with the standard deviation in one-class anomaly detection on two tabular datasets. The best two results are marked in **bold**.

	Thyroid	Arrhythmia
OCSVM Schölkopf et al. [1999]	0.56 ± 0.01	0.64 ± 0.01
Deep SVDD Ruff et al. [2018]	0.73 ± 0.00	0.54 ± 0.01
LOF Breunig et al. [2000]	0.54 ± 0.01	0.51 ± 0.01
GOAD Bergman and Hoshen [2020]	0.75 ± 0.01	0.52 ± 0.02
DROCC Goyal et al. [2020]	0.78 ± 0.03	0.69 ± 0.02
PLAD Cai and Fan [2022]	0.77 ± 0.01	0.71 ± 0.02
DOHSC	0.92 ± 0.01	0.70 ± 0.03
DO2HSC	0.88 ± 0.03	0.74 ± 0.02

Non-graph experimental results are reported in Tables 4 and 5. First, Table 4 summarizes the F1-scores of all competitive methods on Thyroid and Arrhythmia datasets. It can be seen a significant margin between the baselines and ours, especially the 92% performance of DOHSC on the Thyroid. Even if there exists the difficulty of a small sample size on Arrhythmia data, DO2HSC still surpasses 2% compared to PLAD. On Fashion-MNIST dataset, DOHSC and DO2HSC obtained seven best AUCs out of ten in total. And in the remaining three classes, the proposed models still achieved comparable performance with gaps of less than 2%. The complete results on Fashion-MNIST (with standard

Table 5: Average AUCs in one-class anomaly detection on Fashion-MNIST. The best performance is highlighted in **bold**.

Normal Class	Deep SVDD	DROCC	FCDD	DOHSC	DO2HSC
T-shirt	0.8263	0.8931	0.8143	0.9153	0.9196
Trouser	0.9632	0.9835	0.9855	0.9817	0.9839
Pullover	0.7885	0.8656	0.8423	0.8007	0.8768
Dress	0.8607	0.8776	0.9143	0.9178	0.9171
Coat	0.8417	0.8453	0.8607	0.8805	0.9038
Sandal	0.8902	0.9336	0.9089	0.8932	0.9308
Shirt	0.7507	0.7789	0.7750	0.8177	0.8022
Sneaker	0.9676	0.9624	0.9874	0.9678	0.9677
Bag	0.9039	0.7797	0.8584	0.9122	0.9090
Ankle Boot	0.9488	0.9589	0.9432	0.9756	0.9785

deviation) can be referred in Appendix F. Second, Deep SVDD plays an important baseline role relative to DOHSC. But DOHSC defeats it by a large margin in all classes on non-graph datasets. It further verifies that the proposed orthogonal projection is constructive. Besides, bi-hypersphere learning also performs sufficiently, which fully demonstrates our applicability on non-graph data.

7 Conclusion

This paper has proposed two novel end-to-end graph-level AD methods, DOHSC and DO2HSC, which combined the effectiveness of mutual information between node-level and global features to learn graph representation and the power of hypersphere compression. DOHSC and DO2HSC mitigate the possible shortcomings of hypersphere boundary learning by applying an orthogonal projection for global representation. Furthermore, DO2HSC projects normal data between the interval area of two co-centered hyperspheres to significantly alleviate the *soap-bubble* issue. We also extended DOHSC and DO2HSC to other data types, i.e. image data and tabular data. Comprehensive experimental results strongly demonstrate the superiority of DOHSC and DO2HSC on multifarious datasets. In the future, an interesting direction could be inspecting the reason behind serious *soap-bubble* issue in GAD tasks.

References

Charu C Aggarwal. *An introduction to outlier analysis*. 2017.

Guansong Pang, Chunhua Shen, Longbing Cao, and Anton Van Den Hengel. Deep learning for anomaly detection: A review. *ACM Computing Surveys (CSUR)*, 54(2):1–38, 2021.

Naeem Seliya, Azadeh Abdollah Zadeh, and Taghi M Khoshgoftaar. A literature review on one-class classification and its potential applications in big data. *Journal of Big Data*, 8(1):1–31, 2021.

Lukas Ruff, Robert Vandermeulen, Nico Goernitz, Lucas Deecke, Shoaib Ahmed Siddiqui, Alexander Binder, Emmanuel Müller, and Marius Kloft. Deep one-class classification. In *International Conference on Machine Learning*, pages 4393–4402, 2018.

Sachin Goyal, Aditi Raghunathan, Moksh Jain, Harsha Vardhan Simhadri, and Prateek Jain. DROCC: deep robust one-class classification. In *Proceedings of the 37th International Conference on Machine Learning*, volume 119 of *Proceedings of Machine Learning Research*, pages 3711–3721, 2020.

Yuanhong Chen, Yu Tian, Guansong Pang, and Gustavo Carneiro. Deep one-class classification via interpolated gaussian descriptor. In *Proceedings of the AAAI Conference on Artificial Intelligence*, volume 36, pages 383–392, 2022.

Philipp Liznerski, Lukas Ruff, Robert A. Vandermeulen, Billy Joe Franks, Marius Kloft, and Klaus-Robert Müller. Explainable deep one-class classification. In *Proceedings of the 9th International Conference on Learning Representations*, 2021.

Kihyuk Sohn, Chun-Liang Li, Jinsung Yoon, Minho Jin, and Tomas Pfister. Learning and evaluating representations for deep one-class classification. In *Proceedings of the 9th International Conference on Learning Representations*, 2021.

Linshu Ouyang, Yongzheng Zhang, and Yipeng Wang. Unified graph embedding-based anomalous edge detection. In *International Joint Conference on Neural Networks*, pages 1–8, 2020.

Linchuan Xu, Xiaokai Wei, Jiannong Cao, and Philip S Yu. Icane: Interaction content-aware network embedding via co-embedding of nodes and edges. *International Journal of Data Science and Analytics*, 9(4):401–414, 2020.

Mengxiao Zhu and Haogang Zhu. Mixedad: A scalable algorithm for detecting mixed anomalies in attributed graphs. In *Proceedings of the AAAI Conference on Artificial Intelligence*, volume 34, pages 1274–1281, 2020.

Aleksandar Bojchevski and Stephan Günnemann. Bayesian robust attributed graph clustering: Joint learning of partial anomalies and group structure. In *Proceedings of the AAAI Conference on Artificial Intelligence*, volume 32, 2018.

Haibo Wang, Chuan Zhou, Jia Wu, Weizhen Dang, Xingquan Zhu, and Jilong Wang. Deep structure learning for fraud detection. In *IEEE International Conference on Data Mining*, pages 567–576, 2018.

Mengyu Zheng, Chuan Zhou, Jia Wu, Shirui Pan, Jinqiao Shi, and Li Guo. Fraudne: A joint embedding approach for fraud detection. In *International Joint Conference on Neural Networks*, pages 1–8, 2018.

Panpan Zheng, Shuhan Yuan, Xintao Wu, Jun Li, and Aidong Lu. One-class adversarial nets for fraud detection. In *Proceedings of the AAAI Conference on Artificial Intelligence*, volume 33, pages 1286–1293, 2019.

Raghavendra Chalapathy, Edward Toth, and Sanjay Chawla. Group anomaly detection using deep generative models. In *Joint European Conference on Machine Learning and Knowledge Discovery in Databases*, pages 173–189, 2018.

Bernhard Schölkopf, Robert C. Williamson, Alexander J. Smola, John Shawe-Taylor, and John C. Platt. Support vector method for novelty detection. In *Advances in Neural Information Processing Systems*, pages 582–588, 1999.

Rongrong Ma, Guansong Pang, Ling Chen, and Anton van den Hengel. Deep graph-level anomaly detection by glocal knowledge distillation. In *Proceedings of the Fifteenth ACM International Conference on Web Search and Data Mining*, pages 704–714, 2022.

Lingxiao Zhao and Leman Akoglu. On using classification datasets to evaluate graph outlier detection: Peculiar observations and new insights. *Big Data*, 2021.

Chen Qiu, Marius Kloft, Stephan Mandt, and Maja Rudolph. Raising the bar in graph-level anomaly detection. In Luc De Raedt, editor, *Proceedings of the Thirty-First International Joint Conference on Artificial Intelligence*, pages 2196–2203, 2022.

Roman Vershynin. *High-dimensional probability: An introduction with applications in data science*, volume 47. Cambridge university press, 2018.

Keyulu Xu, Weihua Hu, Jure Leskovec, and Stefanie Jegelka. How powerful are graph neural networks? In *Proceedings of the 7th International Conference on Learning Representations*, 2019.

Fan-Yun Sun, Jordan Hoffmann, Vikas Verma, and Jian Tang. Infograph: Unsupervised and semi-supervised graph-level representation learning via mutual information maximization. In *Proceedings of the 8th International Conference on Learning Representations*, 2020.

Sebastian Nowozin, Botond Cseke, and Ryota Tomioka. f-gan: Training generative neural samplers using variational divergence minimization. In *Advances in Neural Information Processing Systems*, volume 29, 2016.

Svante Wold, Kim Esbensen, and Paul Geladi. Principal component analysis. *Chemometrics and intelligent laboratory systems*, 2(1-3):37–52, 1987.

Beatrice Laurent and Pascal Massart. Adaptive estimation of a quadratic functional by model selection. *Annals of Statistics*, pages 1302–1338, 2000.

Thomas Gärtner, Peter Flach, and Stefan Wrobel. On graph kernels: Hardness results and efficient alternatives. In *Learning Theory and Kernel Machines*, pages 129–143. 2003.

Hisashi Kashima, Koji Tsuda, and Akihiro Inokuchi. Marginalized kernels between labeled graphs. In *Proceedings of the 20th International Conference on Machine Learning*, pages 321–328, 2003.

Karsten M Borgwardt and Hans-Peter Kriegel. Shortest-path kernels on graphs. In *Proceedings of the Fifth IEEE International Conference on Data Mining*, pages 8–pp, 2005.

Nino Shervashidze, Pascal Schweitzer, Erik Jan Van Leeuwen, Kurt Mehlhorn, and Karsten M Borgwardt. Weisfeiler-lehman graph kernels. *Journal of Machine Learning Research*, 12(9), 2011.

Shohei Hido and Hisashi Kashima. A linear-time graph kernel. In *Ninth IEEE International Conference on Data Mining*, pages 179–188, 2009.

Bo Zong, Qi Song, Martin Renqiang Min, Wei Cheng, Cristian Lumezanu, Dae-ki Cho, and Haifeng Chen. Deep autoencoding gaussian mixture model for unsupervised anomaly detection. In *Proceedings of the 6th International Conference on Learning Representations*, 2018.

Liron Bergman and Yedid Hoshen. Classification-based anomaly detection for general data. In *Proceedings of the 8th International Conference on Learning Representations*, 2020.

Markus M. Breunig, Hans-Peter Kriegel, Raymond T. Ng, and Jörg Sander. LOF: identifying density-based local outliers. In *Proceedings of the ACM SIGMOD International Conference on Management of Data*, pages 93–104, 2000.

Jinyu Cai and Jicong Fan. Perturbation learning based anomaly detection. In *Advances in Neural Information Processing Systems*, 2022.

Nils M Kriege, Fredrik D Johansson, and Christopher Morris. A survey on graph kernels. *Applied Network Science*, 5(1):1–42, 2020.

Bernhard Schölkopf, Robert C Williamson, Alex Smola, John Shawe-Taylor, and John Platt. Support vector method for novelty detection. *Advances in neural information processing systems*, 12, 1999.

Max Welling and Thomas N Kipf. Semi-supervised classification with graph convolutional networks. In *Proceedings of the 5th International Conference on Learning Representations*, 2016.

Bernhard Schölkopf, John C Platt, John Shawe-Taylor, Alex J Smola, and Robert C Williamson. Estimating the support of a high-dimensional distribution. *Neural Computation*, 13(7):1443–1471, 2001.

Giannis Siglidis, Giannis Nikolentzos, Stratis Limnios, Christos Giatsidis, Konstantinos Skianis, and Michalis Vazirgiannis. Grakel: A graph kernel library in Python. *Journal of Machine Learning Research*, 21(54):1–5, 2020.

F. Pedregosa, G. Varoquaux, A. Gramfort, V. Michel, B. Thirion, O. Grisel, M. Blondel, P. Prettenhofer, R. Weiss, V. Dubourg, J. Vanderplas, A. Passos, D. Cournapeau, M. Brucher, M. Perrot, and E. Duchesnay. Scikit-learn: Machine learning in Python. *Journal of Machine Learning Research*, 12:2825–2830, 2011.

A Supplemented Algorithm

Algorithm 1 summarizes the procedure of DOHSC in detail. It starts with graph representation learning and promotes the training data to approximate the center of a hypersphere while adding an orthogonal projection layer. Also, DO2HSC is recapped in Algorithm 2 and also starts with same graph representation learning. Differently, DOHSC is utilized of few epochs to initial the decision boundaries and after that, improved optimization is applied.

Algorithm 1 Graph-Level Deep Orthogonal Hypersphere Contraction (DOHSC)

Input: The input graph set \mathbb{G} , dimensions of GIN hidden layers k and orthogonal projection layer k' , a trade-off parameter λ and the coefficient of regularization term μ , pretraining epoch \mathcal{T} , learning rate η .
Output: The anomaly detection scores s .

- 1: Initialize the network parameters Φ, Ψ, Υ and the orthogonal projection layer parameter Θ ;
- 2: **for** $t \rightarrow \mathcal{T}$ **do**
- 3: **for** each batch \mathbf{G} **do**
- 4: Calculate $I_{\Phi, \Psi, \Upsilon}(\mathbf{h}_{\Phi, \Upsilon}, \mathbf{H}_{\Phi, \Psi}(\mathbf{G}))$ via (4);
- 5: Back-propagation GIN and update Φ, Ψ and Υ , respectively;
- 6: **end for**
- 7: **end for**
- 8: Update the orthogonal parameter Θ of orthogonal projection layer by (9);
- 9: Obtain the global orthogonal latent representation by (8);
- 10: Initialize the center of hypersphere by (10);
- 11: **repeat**
- 12: **for** each batch \mathbf{G} **do**
- 13: Calculate total loss via 11;
- 14: Back-propagation and update Φ, Ψ, Υ and Θ , respectively;
- 15: Further update the orthogonal parameter Θ of orthogonal projection layer by (9);
- 16: **end for**
- 17: **until** convergence
- 18: Compute decision boundary r by (12);
- 19: Calculate the anomaly detection scores s through (13);
- 20: **return** The anomaly detection scores s .

B Related Proof of Bi-Hypersphere Learning Motivation

The traditional idea of detecting outliers is to inspect the distribution's tails with an ideal assumption that the normal data are Gaussian. Following the assumption, one may argue that an anomalous sample can be distinguished by its large Euclidean distance to the data center (ℓ_2 norm $\|\mathbf{z} - \mathbf{c}\|$, where \mathbf{c} denotes the centroid), and accordingly, the abnormal dataset is $\{\mathbf{z} : \|\mathbf{z} - \mathbf{c}\| > r\}$ for some decision boundary r . However in high dimensional space, Gaussian distributions look like soap-bubble⁴, which means the normal data are more likely to locate in a bi-hypersphere[Vershynin, 2018], such as $\{\mathbf{z} : r_{\min} < \|\mathbf{z} - \mathbf{c}\| < r_{\max}\}$. To better understand this counterintuitive behavior, let us generate some normal samples $\mathbf{X} \sim \mathcal{N}(\mathbf{0}, \mathbf{I}_d)$, where d is the data dimension in $\{1, 10, 50, 100, 200, 500\}$. As Figure 4 indicates, only the univariate Gaussian has a near-zero mode, whereas other high-dimensional Gaussian distributions leave plenty of offcenter spaces in blank. The soap-bubble problem in high-dimensional distributions is well demonstrated in Table 6: the higher the dimension is, the greater the quantities of data further away from the center, especially for 0.01-quantile distance. Thus, we cannot make a sanguine assumption that **all** of the normal data locate within some radius of a hypersphere (i.e. $\{\mathbf{z} : \|\mathbf{z} - \mathbf{c}\| < r\}$). Using Lemma 1 of [Laurent and Massart, 2000], we can prove that proposition 1, which matches the values in the Table 6 that when the dimension is larger, normal data are more likely lies away from center.

We also simulate a possible case of outlier detection, in which data are all sampled from 16-dimensional Gaussian with orthogonal covariance: 10,000 normal samples follow $\mathcal{N}(\mathbf{0}, \mathbf{I})$ and the first group of 1,000 outliers are from $\mathcal{N}(\mu_1, \frac{1}{10}\mathbf{I})$, the second group of 500 outliers are from $\mathcal{N}(\mu_2, \mathbf{I})$, and the last group of 2,000 outliers are from $\mathcal{N}(\mu_3, 5\mathbf{I})$. Figure 7 well exemplifies that abnormal data from other distribution (group-1 outliers) could fall into the small distance away from the center of the normal samples.

⁴<https://www.inference.vc/high-dimensional-gaussian-distributions-are-soap-bubble/>

Algorithm 2 Graph-Level Deep Orthogonal Bi-Hypersphere Compression (DO2HSC)

Input: The input graph set \mathbb{G} , dimensions of GIN hidden layers k and orthogonal projection layer k' , a trade-off parameter λ and the coefficient of regularization term μ , pretraining epoch \mathcal{T}_1 , iterations of initializing decision boundaries \mathcal{T}_2 , learning rate η .

Output: The anomaly detection scores \mathbf{s} .

1: Initialize the network parameters Φ, Ψ, Υ and the orthogonal projection layer parameter Θ ;

2: **for** $t \rightarrow \mathcal{T}_1$ **do**

3: **for** each batch \mathbf{G} **do**

4: Calculate $I_{\Phi, \Psi, \Upsilon}(\mathbf{h}_{\Phi, \Upsilon}, \mathbf{H}_{\Phi, \Psi}(\mathbf{G}))$ via (4);

5: Back-propagation GIN and update Φ, Ψ and Υ , respectively;

6: **end for**

7: **end for**

8: Update the orthogonal parameter Θ of orthogonal projection layer by (9);

9: Obtain the global orthogonal latent representation by (8);

10: Initialize the center of hypersphere by (10);

11: **for** $t \rightarrow \mathcal{T}_2$ **do**

12: **for** each batch \mathbf{G} **do**

13: Calculate total loss via 11;

14: Back-propagation and update Φ, Ψ, Υ and Θ , respectively;

15: Further update the orthogonal parameter Θ of orthogonal projection layer by (9);

16: **end for**

17: **end for**

18: Initialize decision boundaries r_{\max} and r_{\min} via (14);

19: **repeat**

20: **for** each batch \mathbf{G} **do**

21: Calculate the improved total loss via 15;

22: Back-propagation and update Φ, Ψ, Υ and Θ , respectively;

23: Further update the orthogonal parameter Θ of orthogonal projection layer by (9);

24: **end for**

25: **until** convergence

26: Calculate the anomaly detection scores \mathbf{s} through (16);

27: **return** The anomaly detection scores \mathbf{s} .

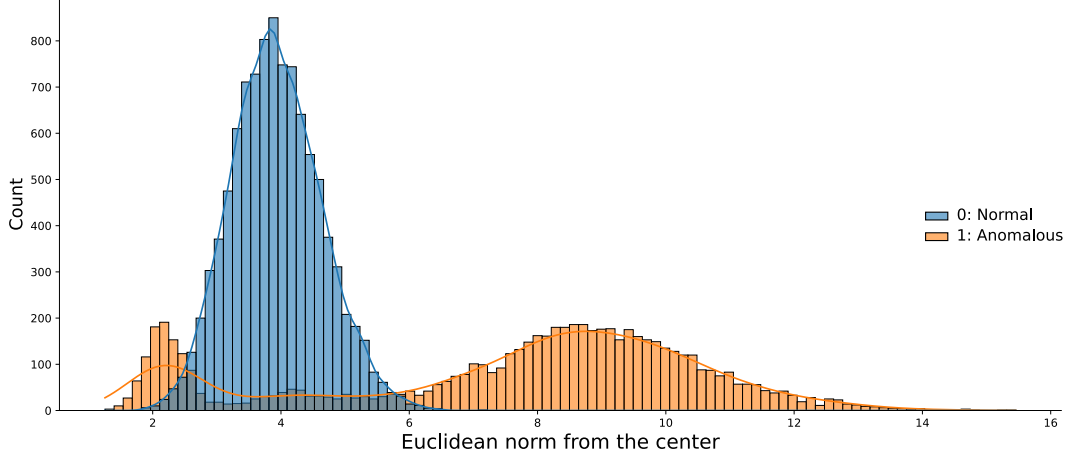


Figure 7: Histogram of distances (Euclidean norm) from the center of normal samples under 16-dimensional Gaussian distributions $\mathcal{N}(\mathbf{0}, \mathbf{I})$. Three groups of anomalous data are also 16-dimensional and respectively sampled from $\mathcal{N}(\mu_1, \frac{1}{10}\mathbf{I})$, $\mathcal{N}(\mu_2, \mathbf{I})$, and $\mathcal{N}(\mu_3, 5\mathbf{I})$, where the population means μ_1, μ_2, μ_3 are randomized within $[0, 1]$ for each dimension.

Table 6: Offcenter distance under multivariate Gaussian at different dimensions and quantiles.

Quantile (correspond to r_{\min})	dim=1	dim=10	dim=50	dim=100	dim=200	dim=500
0.01	0.0127	1.5957	5.5035	8.3817	12.5117	20.6978
0.25	0.3115	2.5829	6.5380	9.4908	13.6247	21.8542
0.50	0.6671	3.0504	7.0141	9.9662	14.1054	22.3337
0.75	1.1471	3.5399	7.5032	10.4386	14.5949	22.8200
0.99	2.5921	4.8265	8.7723	11.6049	15.7913	24.0245

C Proof for Proposition 2

Proof. Since f makes \mathbf{s} obey $\mathcal{N}(\bar{\mathbf{c}}, \mathbf{I}_k)$, according to Proposition 1, we have

$$\mathbb{P} \left[\|\mathbf{s} - \bar{\mathbf{c}}\| \geq \sqrt{k - 2\sqrt{kt}} \right] \geq 1 - e^{-t}.$$

Since f is η -Lipschitz, we have

$$\|\mathbf{s} - f(\mathbf{c})\| = \|f(\mathbf{z}) - f(\mathbf{c})\| \leq \eta \|\mathbf{z} - \mathbf{c}\|.$$

It follows that

$$\begin{aligned} \|\mathbf{z} - \mathbf{c}\| &\geq \eta^{-1} \|\mathbf{s} - \bar{\mathbf{c}} + \bar{\mathbf{c}} - f(\mathbf{c})\| \\ &\geq \eta^{-1} (\|\mathbf{s} - \bar{\mathbf{c}}\| - \|\bar{\mathbf{c}} - f(\mathbf{c})\|) \\ &\geq \eta^{-1} (\|\mathbf{s} - \bar{\mathbf{c}}\| - \epsilon). \end{aligned}$$

Now we have

$$\mathbb{P} \left[\|\mathbf{z} - \mathbf{c}\| \geq \eta^{-1} \left(\sqrt{k - 2\sqrt{kt}} - \epsilon \right) \right] \geq 1 - e^{-t}.$$

This finished the proof. \square

D Related Work

To learn with graph-structured data, graph kernels that measure the similarity between graphs become an established and widely-used approach [Kriege et al., 2020]. A large body of work has emerged in the past years, including kernels based on neighborhood aggregation techniques and walks and paths. Shervashidze et al. [2011] introduced Weisfeiler-Lehman (WL) algorithm, a well-known heuristic for graph isomorphism. In Hido and Kashima [2009], Neighborhood Hash kernel was introduced, where the neighborhood aggregation function is binary arithmetic. The most influential graph kernel for paths-based kernels is the shortest-path (SP) kernel by Borgwardt and Kriegel [2005]. For walks-based kernels, Gärtner et al. [2003] and Kashima et al. [2003] simultaneously proposed graph kernels based on random walks, which count the number of label sequences along walks that two graphs have in common. These graph kernel methods have the desirable property that they do not rely on the vector representation of data explicitly but access data only via the Gram matrix.

There are few studies undertaken in graph-level anomaly detection (GAD). Existing solutions to GAD can be categorized into two families: two-stage and end-to-end. Two-stage GAD methods Breunig et al. [2000], Schölkopf et al. [1999] first transform graphs into graph embeddings by graph neural networks or into similarities between graphs by graph kernels, and then apply off-the-shelf anomaly detectors. The drawbacks of it mainly include: 1) the graph feature extractor and outlier detector are independent; 2) some graph kernels produce “hand-crafted” features that are deterministic without much space to improve. Whereas, end-to-end approaches overcome these problems by utilizing deep graph learning techniques (such as graph convolutional network Welling and Kipf [2016] and graph isomorphism network Xu et al. [2019]), which learn an effective graph representation while detecting graph anomaly Zhao and Akoglu [2021], Qiu et al. [2022], Ma et al. [2022].

E Experiment Configuration

In this part, the experiment settings are listed for reproducing. First, each dataset is divided into two parts: training and testing sets. We randomly sample eighty percent of the normal data as the training set, and the remaining normal data together with the randomly sampled abnormal data in a one-to-one ratio to form the testing set. In addition, the detailed statistic information of tested datasets are given in Tables 7 and 8.

Table 7: Description for six graph datasets.

Datasets	# Graphs	Avg. # Nodes	Avg. # Edges	# Classes	# Graph Labels
COLLAB	5000	74.49	2457.78	3	2600 / 775 / 1625
COX2	467	42.43	44.54	2	365 / 102
ER_MD	446	21.33	234.85	2	265 / 181
MUTAG	188	17.93	19.79	2	63 / 125
DD	1178	284.32	715.66	2	691 / 487
IMDB-Binary	1000	19.77	96.53	2	500 / 500

Table 8: Description for non-graph datasets.

Dataset Name	Type	# Instances	# Dimension
Thyroid	Tabular	3772	6
Arrhythmia	Tabular	452	274
Fashion-MNIST	Image	70000	28×28

With regard to the experiment settings of compared graph-kernel baselines, we adopted the classical AD method, One-Class SVM (OCSVM) [Schölkopf et al., 2001] and used 10-fold cross-validation to make a fair comparison. All graph kernels via GraKel [Siglidis et al., 2020] to extract a kernel matrix and apply OCSVM in scikit-learn [Pedregosa et al., 2011] are implemented. Specifically, we selected Floyd Warshall as the SP kernel’s algorithm and set lambda as 0.01 for the RW kernel. WL kernel algorithm is sensitive to the number of iterations, so we test four types with the iteration of {2, 5, 8, 10} and denote them as WL₂, WL₅, WL₈, WL₁₀, and keep the optimal results for each experimental variant. For all graph kernels, the outputs are normalized. About infoGraph+Deep SVDD, the first stage runs in 20 epochs, and the second stage pretrains 50 epochs and trains 100 epochs. In OCGIN, GLocalKD, and OCGTL, their default or reported parameter settings are adopted to reproduce experimental results. But there still exists some special situations like, due to the limited device, the relatively large-scale dataset is tested with a small batch size, such as DD. This may lead to worse performance for compared algorithms.

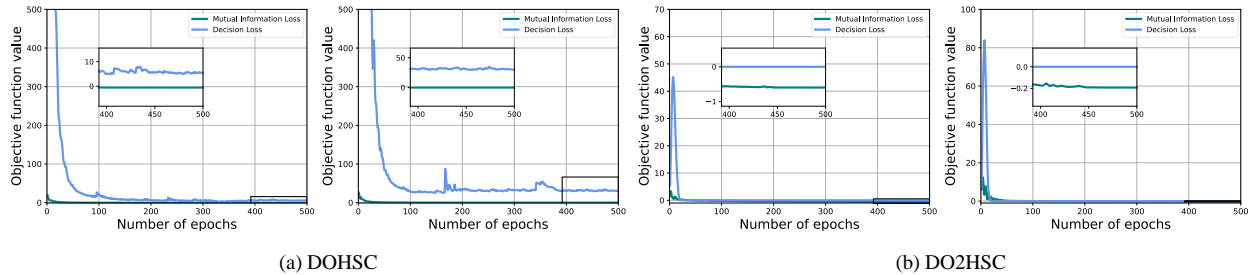


Figure 8: Convergence curves of the proposed models on the MUTAG dataset.

Regarding our model DOHSC, we firstly set 1 epoch in the pretraining stage to initialize the center of the decision boundary and then train the model in 500 epochs. The convergence curves are given in Figure 8 to indicate that the final optimized results are adopted. The improved method DO2HSC is also set 1-epoch pretraining stage and trains DOHSC 5 epochs to initialize a suitable center and decision boundaries r_{\max} and r_{\min} , where the percentile ν of r_{\max} is selected as 0.01. After initializing, the model is trained in 500 epochs. For both proposed approaches, the trade-off factor λ is set to 10 to ensure decision loss as the main optimization objective. Dimensions of the GIN hidden layer and orthogonal projection layer are fixed as 16 and 8, respectively. About the backbone network, a 4-layer GIN and a 3-layer fully connected neural network are adopted. Besides, the averages and standard deviations of the Area Under Operating Characteristic Curve (AUC) are used to support the comparable experiments by repeating each algorithm ten times. The higher value of the AUC metric represents better performance. When calculating the AUC of graph-kernel baselines, we estimated the radius of the hypersphere as 99 percentile of all squared distances to the separating hyperplane and then determined the score as the difference between squared distances and its square radius. Regarding our model DOHSC, we firstly set 1 epoch in the pretraining stage to initialize the center of the decision boundary and then train

the model in 500 epochs. The convergence curves are given in Figure 8. The improved method DO2HSC is also set 1-epoch pretraining stage and trains DOHSC 5 epochs to initialize a suitable center and decision boundaries r_{\max} and r_{\min} , where the percentile ν of r_{\max} is selected as 0.01 or 0.05. After initializing, the model is also trained in 500 epochs. For both proposed approaches, the trade-off factor λ is set to 10. Dimensions of the GIN hidden layer and orthogonal projection layer are fixed as 16 and 8, respectively. About the backbone network, a 4-layer GIN and a 3-layer fully connected neural network are adopted. Besides, the averages and standard deviations of the Area Under Operating Characteristic Curve (AUC) are used to support the comparable experiments by repeating each algorithm ten times. The higher value of the AUC metric represents better performance. When calculating the AUC of graph-kernel baselines, we estimated the radius of the hypersphere as 99 percentile of all squared distances to the separating hyperplane and then determined the score as the difference between squared distances and its square radius.

F Supplemented Results on Fashion-MNIST

The complete experimental results on the Fashion-MNIST image dataset is given in Table 9. Detailed standard deviation can demonstrate the fluctuations of performance. Obviously, the proposed methods are relatively stable, especially DOHSC.

Table 9: Average AUCs in one-class anomaly detection on Fashion-MNIST.

Normal Class	Deep SVDD [Ruff et al., 2018]	DROCC [Goyal et al., 2020]	FCDD [Liznerski et al., 2021]	DOHSC	DO2HSC
T-shirt	0.8263 \pm 0.0342	0.8931 \pm 0.0072	0.8143 \pm 0.0101	0.9153 \pm 0.0082	0.9196 \pm 0.0064
Trouser	0.9632 \pm 0.0072	0.9835 \pm 0.0054	0.9855 \pm 0.0014	0.9817 \pm 0.0060	0.9839 \pm 0.0020
Pullover	0.7885 \pm 0.0398	0.8656 \pm 0.0140	0.8423 \pm 0.0052	0.8007 \pm 0.0204	0.8768 \pm 0.0122
Dress	0.8607 \pm 0.0124	0.8776 \pm 0.0269	0.9143 \pm 0.0120	0.9178 \pm 0.0230	0.9171 \pm 0.0084
Coat	0.8417 \pm 0.0366	0.8453 \pm 0.0143	0.8607 \pm 0.0213	0.8805 \pm 0.0258	0.9038 \pm 0.0140
Sandal	0.8902 \pm 0.0281	0.9336 \pm 0.0123	0.9089 \pm 0.0165	0.8932 \pm 0.0287	0.9308 \pm 0.0070
Shirt	0.7507 \pm 0.0158	0.7789 \pm 0.0188	0.7750 \pm 0.0038	0.8177 \pm 0.0124	0.8022 \pm 0.0045
Sneaker	0.9676 \pm 0.0062	0.9624 \pm 0.0059	0.9874 \pm 0.0007	0.9678 \pm 0.0050	0.9677 \pm 0.0075
Bag	0.9039 \pm 0.0355	0.7797 \pm 0.0749	0.8584 \pm 0.0222	0.9122 \pm 0.0258	0.9090 \pm 0.0105
Ankle Boot	0.9488 \pm 0.0207	0.9589 \pm 0.0207	0.9432 \pm 0.0050	0.9756 \pm 0.0127	0.9785 \pm 0.0038

G Supplemented Visualization

This part shows the related supplemented visualization results of the anomaly detection task. From Section 5, we can see some DOHSC results are improved a lot through DO2HSC. For example, compared with DOHSC, DO2HSC often improves the results by less than 2% on most of the datasets. But on class 1 of ER_MD, DO2HSC has a more than 20% improvement. Here the distance distributions of DOHSC and DO2HSC on ER_MD are given in Figure 5 to prove this improvement. In Subfigure (a), the anomalous data appear in the distance interval [0,1], especially in the region close to the center, and less or even none of the normal data distributes in it. On the contrary, DO2HSC divided normal data and anomalous data more specifically, and both sides of the interval have anomalous data, as we assumed before.

Figure 9 shows the distance distributions of the two-stage method, the proposed model DOHSC, and the improved DO2HSC. Here, the *distance* is defined as the distance between the sample and the center of the decision hypersphere. The distance distribution denotes the sample proportion in this distance interval to the corresponding total samples. It can be intuitively observed that most distances of instances are close to the decision boundary because of the fixed learned representation. As mentioned earlier, the jointly-trained algorithm has mitigated the situation, and the obtained representation makes many instances have smaller distances from the center of the sphere.

However, like we wrote in Section 2, anomalous data may occur in regions with less training data, especially the region close to the center, which is also confirmed by (a) and (b) of Figure 9. Differently, DO2HSC effectively shrinks the decision area, and we find that the number of outliers is obviously reduced due to a more compact distribution of training data.

G.1 Parameter Sensitivity and Robustness

To claim the stability of our models, we analyze the parameter sensitivity and robustness of DOHSC and DO2HSC, respectively. Consider that the projection dimension varies in $\{4, 8, 16, 32, 64, 128\}$ while the hidden layer dimension of the GIN module ranges from 4 to 128. In Figure 11, the DO2HSC model has less volatile performances than DOHSC, especially when the training dataset is sampled from COX2 class 0, as Subfigure (d) shows. Noticeably, a higher dimension of the GIN hidden layer usually displays a better AUC result since the quality of learned graph representations improves when the embedding space is large enough.

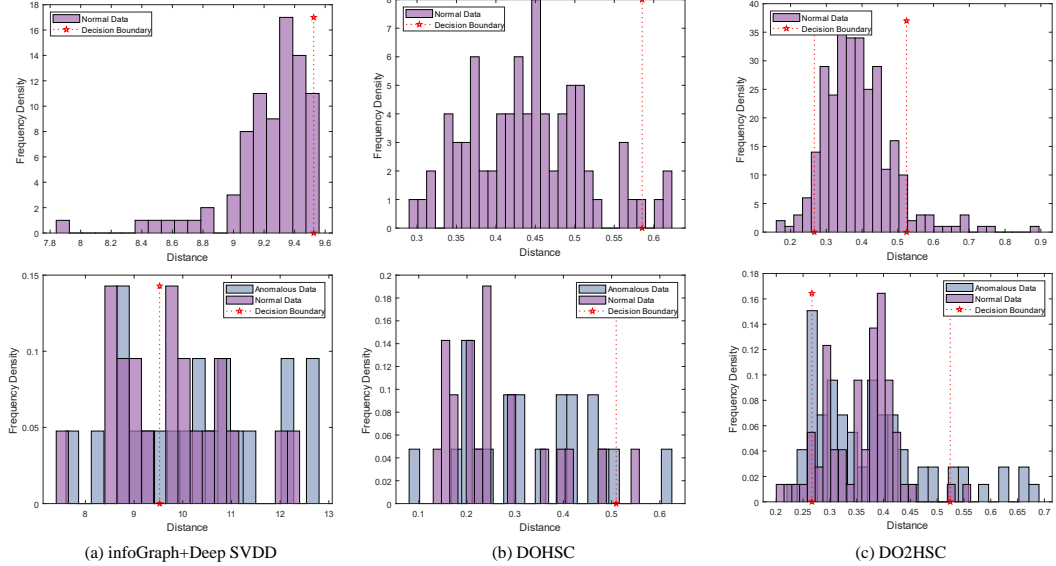


Figure 9: Distance distributions were obtained by infoGraph+Deep SVDD, the proposed model, and the improved proposed model on COX2. The first row represents the distance distribution of the training samples in relation to the decision boundary. The last row indicates the distance distribution of the test data with respect to the decision boundary.

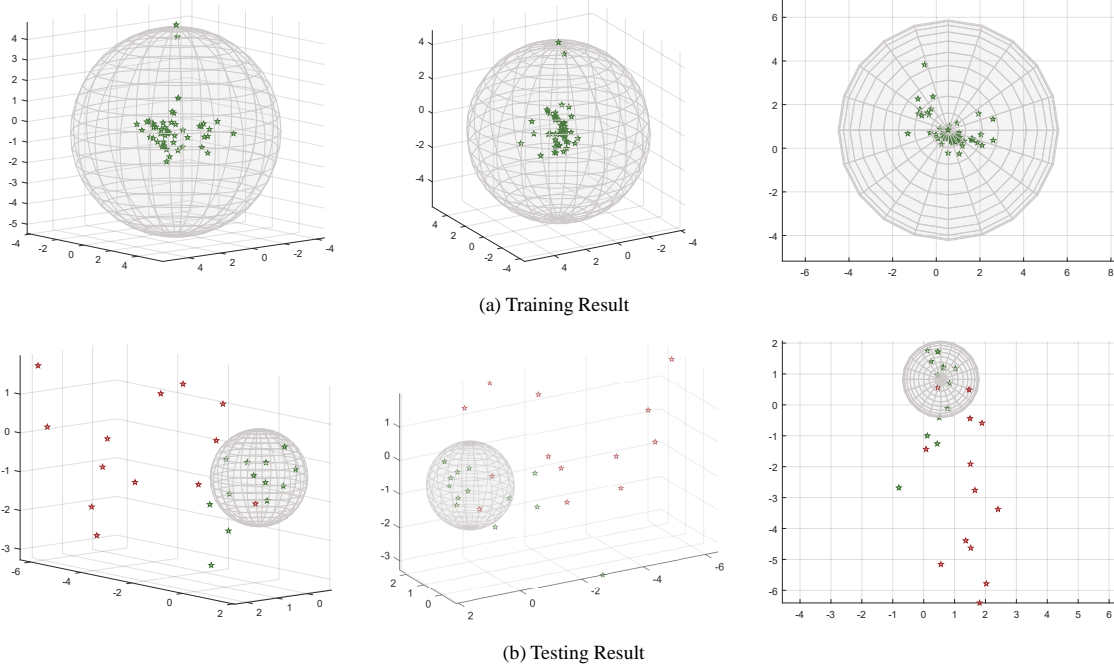


Figure 10: Visualization results of the DOHSC with MUTAG in different perspectives.

In addition, we assess different aspects of model robustness. More specifically, the AUC results about two "ratios" are displayed: 1) Different sampling ratios for the training set; 2) Different ratios of noise disturbance for the learned representation. In Subfigures (c) (f), the purple bars regard normal data as class 0, while green bars treat normal data as class 1. Notice that most AUC results are elevating along with a higher ratio of authentic data in the training stage, demonstrating our models' potential in the unsupervised setting. On the other hand, when more noise is blended into the training dataset, the AUC performances of yellow line and blue line always stay stable at a high level. This outcome verifies our models' robustness in response to the alien data.

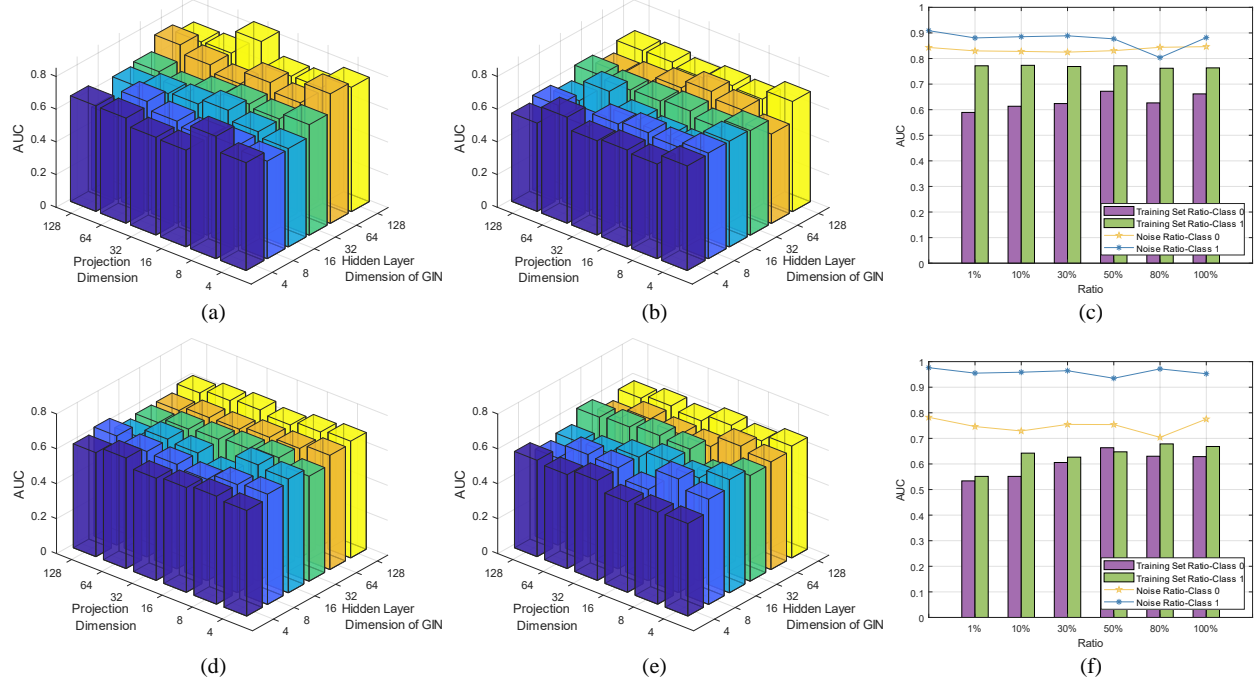


Figure 11: Parameter sensitivity and robustness of the proposed models. (a)-(b) Parameter sensitivity of DOHSC with different hidden layer dimensions of GIN and projection dimensions on COX2 with Class 0 and Class 1, respectively. (d)-(e) Parameter sensitivity of DO2HSC with the same settings. (c) and (f) shows the performance impacts with different ratios of the training set on the IMDB-Binary dataset and added noise disturbances on the MUTAG dataset while training DOHSC and DO2HSC, respectively.

The percentile parameter sensitivity is also given in this part. It is worth mentioning that we test DOHSC with varying percentile in $\{0.01, 0.1, \dots, 0.8\}$ and test DO2HSC only in $\{0.01, 0.05, 0.1\}$ because two radii of DO2HSC is obtained by percentile ν and $1 - \nu$. Two radii will be equal when $\nu = 0.5$ and the interval between two co-centered hyperspheres will disappear. From the table, the performance would decrease when a larger percentile is set obviously. For example, on the MUTAG dataset, setting the percentile as 0.01 is more beneficial for DOHSC than setting it as 0.8, and setting the percentile as 0.01 is better than setting it as 0.1 for DO2HSC due to the change of the interval area.

Table 10: Parameter sensitivity of **DOHSC** with different percentiles (all normal data is set to Class 0.)

Dataset	Percentile				
	0.005	0.01	0.1	0.5	0.8
COX2	0.5446 (0.0854)	0.6263 (0.0333)	0.6022 (0.0789)	0.5232 (0.0494)	0.5523 (0.0572)
ER_MD	0.6265 (0.1442)	0.6620 (0.0308)	0.7497 (0.0411)	0.6265 (0.1442)	0.5141 (0.0398)
MUTAG	0.8185 (0.0543)	0.8822 (0.0432)	0.8540 (0.0694)	0.7790 (0.0912)	0.8675 (0.1287)
DD	0.6349 (0.0380)	0.7083 (0.0188)	0.6597 (0.0270)	0.6545 (0.0268)	0.6327 (0.0206)
IMDB-Binary	0.7232 (0.0314)	0.7160 (0.0600)	0.7217 (0.0418)	0.7073 (0.0274)	0.6773 (0.0566)

Table 11: Parameter sensitivity of **DO2HSC** with different percentiles (all normal data is set to Class 0.)

Dataset	Percentile			
	0.005	0.01	0.05	0.1
COX2	0.5810 (0.0354)	0.6329 (0.0292)	0.6149 (0.0187)	0.5830 (0.0713)
ER_MD	0.6136 (0.0769)	0.6226 (0.0890)	0.6867 (0.0226)	0.6331 (0.1748)
MUTAG	0.7278 (0.0478)	0.9089 (0.0609)	0.8041 (0.1006)	0.6769 (0.1207)
DD	0.7103 (0.0098)	0.7320 (0.0194)	0.6909 (0.0208)	0.6765 (0.0286)
IMDB-Binary	0.6590 (0.0287)	0.6406 (0.0642)	0.5348 (0.0486)	0.5701 (0.0740)

H Supplemented Results of Ablation Study

First, the ablation study of whether orthogonal projection needs standardization is conducted. To be more precise, we are pursuing orthogonal features, i.e., finding a projection matrix for orthogonal latent representation (with standardization) instead of computing the projection onto the column or row space of the projection matrix (non-standardization), though they are closely related to each other. This is equivalent to performing PCA and using the standardized principal components. Therefore, we show the comparison between DOHSC with standardization and without standardization. From Table 12, it is observed that the performance of DOHSC without standardization is acceptable and most results of it are better than the two-stage baseline, i.e., infoGraph+Deep SVDD. It verifies the superiority of the end-to-end method over the two-stage baselines. However, the model with standardization outperforms the non-standardized one in almost all cases.

Table 12: Comparison of the orthogonal projection layer with or w/o standardization.

	Class	infoGraph+Deep SVDD	DOHSC (Non-Standardization)	DOHSC
MUTAG	0	0.8805 ± 0.0448	0.8521 ± 0.0650	0.8822 ± 0.0432
	1	0.6166 ± 0.2052	0.6918 ± 0.1467	0.8115 ± 0.0279
COX2	0	0.4825 ± 0.0624	0.5800 ± 0.0473	0.6263 ± 0.0333
	1	0.5029 ± 0.0700	0.5029 ± 0.0697	0.6805 ± 0.0168
ER_MD	0	0.5312 ± 0.1545	0.4881 ± 0.0626	0.6620 ± 0.0308
	1	0.5682 ± 0.0704	0.6740 ± 0.0356	0.5184 ± 0.0793
DD	0	0.3942 ± 0.0436	0.4029 ± 0.0354	0.7083 ± 0.0188
	1	0.6484 ± 0.0236	0.6903 ± 0.0215	0.7579 ± 0.0154
IMDB-Binary	0	0.6353 ± 0.0277	0.5149 ± 0.0655	0.6609 ± 0.0033
	1	0.5836 ± 0.0995	0.6505 ± 0.0585	0.7705 ± 0.0045
COLLAB	0	0.5662 ± 0.0597	0.6067 ± 0.1007	0.9185 ± 0.0455
	1	0.7926 ± 0.0986	0.8958 ± 0.0141	0.9755 ± 0.0030
	2	0.4062 ± 0.0978	0.4912 ± 0.2000	0.5450 ± 0.0469

Besides, the ablation study of using the mutual information maximization loss is shown in Table 13. It can be intuitively concluded that mutual information loss does not always have a positive impact on all data. This also indicates that the anomaly detection optimization method and orthogonal projection we designed are effective instead of entirely due to the loss of mutual information.

Table 13: Comparison of the loss supervision with or w/o **mutual information loss (MIL)**.

	Class	DOHSC (Non-MIL)	DOHSC	DO2HSC (Non-MIL)	DO2HSC
MUTAG	0	0.9456 ± 0.0189	0.8822 ± 0.0432	0.8308 ± 0.0548	0.9089 ± 0.0609
	1	0.7597 ± 0.0802	0.8115 ± 0.0279	0.7915 ± 0.0274	0.8250 ± 0.0790
COX2	0	0.6349 ± 0.0466	0.6263 ± 0.0333	0.6143 ± 0.0302	0.6329 ± 0.0292
	1	0.6231 ± 0.0501	0.6805 ± 0.0168	0.6576 ± 0.1830	0.6518 ± 0.0481
ER_MD	0	0.5837 ± 0.0778	0.6620 ± 0.0308	0.5836 ± 0.0909	0.6867 ± 0.0226
	1	0.6465 ± 0.0600	0.5184 ± 0.0793	0.7424 ± 0.0385	0.7351 ± 0.0159
DD	0	0.4738 ± 0.0412	0.7083 ± 0.0188	0.6882 ± 0.0221	0.7320 ± 0.0194
	1	0.7197 ± 0.0185	0.7579 ± 0.0154	0.7376 ± 0.0244	0.7651 ± 0.0317
IMDB-Binary	0	0.5666 ± 0.0810	0.6609 ± 0.0033	0.6303 ± 0.0538	0.6406 ± 0.0642
	1	0.6827 ± 0.0239	0.7705 ± 0.0045	0.6810 ± 0.0276	0.7101 ± 0.0429
COLLAB	0	0.9330 ± 0.0539	0.9185 ± 0.0455	0.5415 ± 0.0182	0.6718 ± 0.0353
	1	0.9744 ± 0.0017	0.9755 ± 0.0030	0.9293 ± 0.0023	0.9153 ± 0.0070
	2	0.8275 ± 0.0765	0.5450 ± 0.0469	0.8452 ± 0.0243	0.7188 ± 0.0260

To demonstrate the effectiveness of the orthogonal projection layer (OPL), we conduct ablation studies and visualize the comparison of 3-dimensional results produced with OPL and without OPL, respectively. For each model trained on

a particular dataset class, we show the result without OPL on the left side, while the result with OPL is displayed on the right. As Figure 12 illustrates, OPL drastically improves the distribution of the embeddings to be more spherical rather than elliptical. Similarly, with the help of OPL, other embeddings show a more compact and rounded layout.

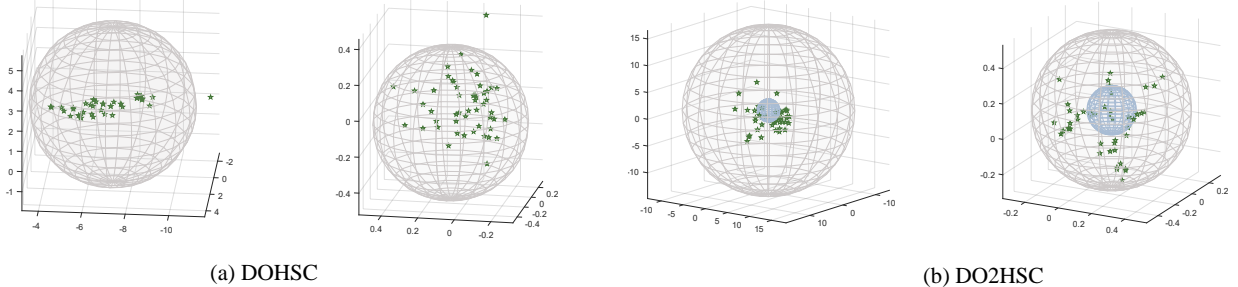


Figure 12: Visualizations on the MUTAG dataset Class 0 (left: with OPL; right: without OPL).

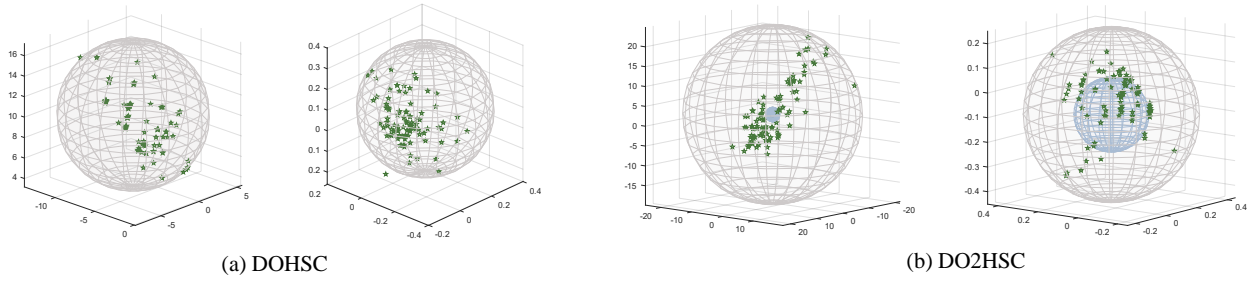


Figure 13: Visualizations on the MUTAG dataset Class 1 (left: with OPL; right: without OPL).

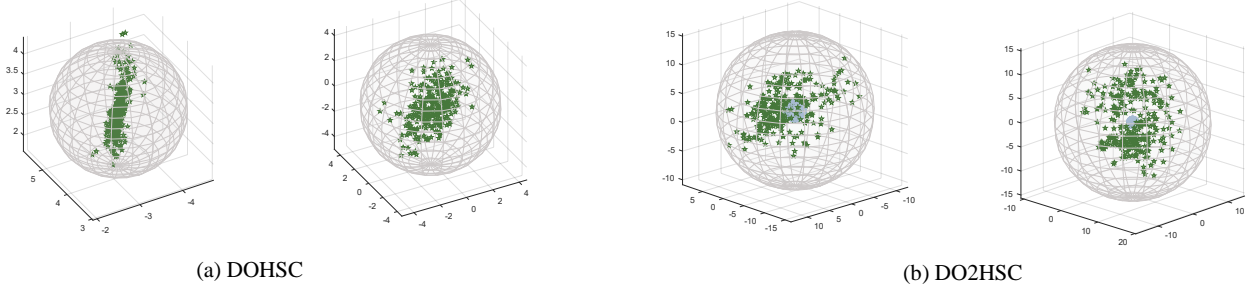


Figure 14: Visualizations on the COX2 dataset Class 0 (left: with OPL; right: without OPL).

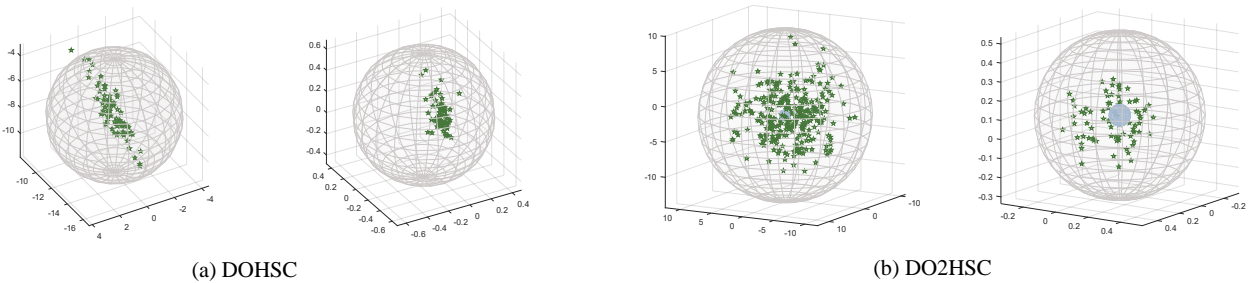


Figure 15: Visualizations on the COX2 dataset Class 1 (left: with OPL; right: without OPL).